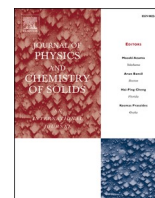




Contents lists available at ScienceDirect

Journal of Physics and Chemistry of Solids

journal homepage: <http://www.elsevier.com/locate/jpcs>

Phase transition, electronic transitions and visible light driven enhanced photocatalytic activity of Eu–Ni co-doped bismuth ferrite nanoparticles

Subhra S. Brahma^a, Jyotirmayee Nanda^{b,*}, Naresh K. Sahoo^c, B. Naik^c, Anup Anang Das^c^a Centre for Nano Science and Nano Technology, ITER, S'O'A Deemed to be University, Khandagiri, Bhubaneswar, 751030, Odisha, India^b Department of Physics, ITER, S'O'A Deemed to be University, Khandagiri, Bhubaneswar, 751030, Odisha, India^c Department of Chemistry, ITER, S'O'A Deemed to be University, Khandagiri, Bhubaneswar, 751030, Odisha, India

ARTICLE INFO

Keywords:

Eu–Ni co-Doped bismuth ferrite
Sol-gel synthesis
Structural analysis
Optical analysis
Photocatalysis

ABSTRACT

This article focusses on the detailed structural and optical properties of 'Eu' and 'Ni' co-substituted Bismuth Ferrite nanoparticles synthesized using the sol-gel method. Raman analysis have confirmed the substitution induced structural distortion leading to the co-existence of Rhombohedral and Orthorhombic structures supporting the XRD and Rietveld Refinement results. Morphological studies using FESEM and HRTEM have shown irregular and inhomogeneous distribution of particles with presence of mixed phases and the elemental composition is also confirmed through EDAX analysis. The XPS analysis indicated the simultaneous presence of Fe²⁺ and Fe³⁺ states along with Bi³⁺, Eu³⁺ and oxygen vacancies. Thorough optical investigation using UV–Vis and PL Spectroscopy has shown an increase in absorption intensity in the visible region with a bandgap tuning from 2.17 eV to 2.12 eV in the co-substituted nanoparticles. A possible schematic energy band diagram is proposed on the basis of observed transitions in photoluminescence studies, VB-XPS analysis along with the knowledge of optical transitions in d⁵ systems. Photocatalytic performance of the synthesized nanostructures is studied by degradation of 2-nitrophenol. The enhanced photocatalytic response has been explained on the basis of decreased band-gap, space charge thickness and charge carrier recombination.

1. Introduction

In the scientific community, there has been an increase in the demand for multiferroic perovskites due to its diverse practical applications. Among them, Bismuth Ferrite (BiFeO₃) has garnered quite a lot of attention because of its above room temperature co-existence of ferroelectricity and G-type anti-ferromagnetism, low bandgap, low production cost, and high visible light absorption. Due to its interesting fundamental physics, BiFeO₃ (BFO) can have potential applications in various fields, such as data storage, spintronic devices, sensors, photovoltaics, and photocatalysis [1–5]. However, certain limitations such as high leakage current, secondary phase formation, cancellation of macroscopic magnetization in bulk BFO due to its spiral spin period of 62 nm, impedes the practical application of BFO in devices. To overcome these limitations, there have been several reports on partial substitution of A ('Bi') site with rare-earth lanthanides such as La³⁺, Gd³⁺, Nd³⁺, Sm³⁺, Pr⁴⁺, Eu³⁺ etc [6–8] and B ('Fe') site with transition metals such as Mn³⁺, Cu²⁺, Ni²⁺ etc [9–11]. Doping Bi³⁺ with rare-earth ions has resulted in the formation of pure phase compound with an enhancement

of ferroelectric properties of BFO by reducing the volatility of 'Bi' ions. The 4f transitions of rare-earth substituted BFO as catalysts have improved its optical absorbing ability along with supporting the separation of photogenerated charge carriers. The substitution of 'Fe' site with transition metal ions helps in enhancing the multiferroic properties of BFO by destroying its spin cycloid structure.

Recently, researchers have adopted co-doping for better tailoring of magnetoelectric, optical and electrical properties of BFO. The combination of rare-earth elements with transition metal ions such as Nd–Ni, Ho–Ni, Ce–Mn, Eu–Mn, Eu–Co and with alkaline earth metal such as Eu–Ba have shown exemplary results [12–17]. Magnetic properties of Ho–Ni doped BFO have shown no structural distortion with enhanced magnetization values as well as low coercive field [12]. As reported by authors 'Ni' doping plays an important part in the enhancement of ferromagnetic properties whereas 'Ho' favours magnetic exchange interactions. Similarly Neodymium and nickel co-doped BFO exhibit ferroelectric nature at different frequencies. Photocatalytic activity studies using degradation of methylene blue dye, shows that the co-doped samples are good Fenton-like catalysts [14]. With Eu–Mn

* Corresponding author.

E-mail address: jyotirmayeenanda@soa.ac.in (J. Nanda).<https://doi.org/10.1016/j.jpcs.2021.110018>

Received 2 December 2020; Received in revised form 20 February 2021; Accepted 22 February 2021

Available online 27 February 2021

0022-3697/© 2021 Elsevier Ltd. All rights reserved.

doping in BFO, Zhu *et al.* have thoroughly investigated the effect of rare-earth and transition metal co-doping on its structural, optical and magnetic properties [16]. The band-gap substantially reduced from 2.40 eV in pristine BFO to 1.49 eV in Eu–Mn doped samples. The Eu–Mn co-doped nanostructures show distinct morphologies with defined grain boundaries and reduction in grain sizes, indicating suppression of grain growth. Banu *et al.* have reported about the enhancement of multiferroic properties upon co-doping BFO with Er–Nb, Mn, Mo. Among them, Er–Nb doped BFO has shown maximum polarization and highest magnetoelectric coupling as well as lowest leakage current density [18]. The dopants have also altered the surface morphology of flake-like BFO, synthesized using sol-gel method. The co-doped samples have agglomerated non-uniform structures with some flake-like and cylindrical structures. Thus, it can be conjectured that the morphology is greatly affected by the combination of co-dopants. Uman *et al.* have designed La–Se doped BFO with lesser band-gap of 1.76 eV compared to 2.04 eV of BFO and studied its visible-light photocatalytic effect [19]. La–Se doped samples show sheet type morphology with the size of sheets increasing as the ‘Se’ concentration increases. Eu, Tb, Ho–Co dopants on BFO thin films have shown that pores present in pure BFO thin films have substantially reduced and grain size increased, which maybe due to the suppression of oxygen vacancies [20].

However, there have been comparatively fewer studies on its optical properties, interband electronic transitions and its application in photocatalysis for the breaking down of industrial organic pollutants. With detailed studies using absorption spectroscopy and spectroscopic ellipsometry, BFO has shown a low bandgap in the visible range of about 2.2–2.8 eV and high absorption coefficient [13] in comparison to its extensively used wide band-gap semiconductors such as TiO₂ (3.3eV), ZnS (3.6eV) and ZnO (3.4eV) [21–26]. Despite that, the commercialization of BFO in this industry has not been very viable because of its low efficiency. Several techniques such as surface modification, particle size reduction, doping in a small quantity have been employed to enhance the efficiency of BFO as a photocatalytic agent [5]. A small amount of dopant can help to restrict the recombination rate of photo-generated carriers as it acts as trap sites for electrons and thus improves the photocatalytic response [27]. There are several reports on the ameliorated photocatalytic response of BFO on doping, for the degradation of toxic industrial dyes such as Rhodamine B (RhB), methyl orange, methylene blue, congo-red, 4-nitrophenol, etc. Sarkar *et al.* [28] have reported morphology mediated enhanced photocatalytic activity owing to the reduction in band-gap of BFO on substitution of ‘Bi³⁺’ with ‘Dy³⁺’. Degradation of several other industrial dyes such as congo red, methylene blue, and methyl violet were also investigated on doping with Gd³⁺ and Sn⁴⁺ [29,30]. La³⁺ and Se⁴⁺ doping have also increased the photocatalytic efficiency for degradation of acetophenone solution by tailoring the band-gap from 2.06 eV for pure BFO to 1.97 eV for La–Se co-doped BFO [27]. With ‘Gd’ and ‘Sm’ doping, the authors have reported 2.55 times higher photocatalytic response than pure BFO [31]. Nadeem *et al.* [32] have recently discussed the enhanced degradation efficiency of Ni-doped BFO on methylene blue (MB) under visible light irradiation, due to the lower recombination rates of the charge carriers. Compared to an increased number of studies of the photocatalytic response of BFO, for degradation of industrial dyes there are quite scarce reports on the breaking down of phenol and nitrophenol isomers (2-nitrophenol, 4-nitrophenol, 3-nitrophenol) using BFO as photocatalyst [33–35].

A thorough literature survey on the co-doped (lanthanides and transition metal ions) bismuth ferrite has shown that there is no study on the structural, optical or photocatalytic response of BFO on co-doping ‘Eu’ and ‘Ni’ at ‘A’ and ‘B’ sites respectively. This motivated us to study the interplay between the structural transformation and electronic transitions (interband), which eventually would make this a good photocatalyst (visible light responsive) for the degradation of organic pollutants such as 2-nitrophenol. In this paper, we present the structural properties of single-phase Bi_{0.96}Eu_{0.04}Fe_{1-x}Ni_xO₃ (x = 0.03, 0.05, 0.07)

nanoparticles. The co-doping effects on the band-gap tuning, interband electronic transitions and photocatalytic performance of all the samples for the breaking down of 2-nitrophenol are extensively studied.

2. Experimental details

2.1. Synthesis method

The Eu–Ni co-doped bismuth ferrite nanoparticles were synthesized using wet chemical method, which has proved to be cost-effective and a better alternative to the typical solid-state method of sample preparation with certain disadvantages such as high crystallization temperatures and secondary phase formation. For the synthesis of Bi_{0.96}Eu_{0.04}Fe_{1-x}Ni_xO₃ (x = 0.03, 0.05, 0.07) (BEFNO) nanoparticles, Bismuth nitrate pentahydrate (Bi(NO₃)₃·5H₂O), Iron nitrate nonahydrate (Fe(NO₃)₃·9H₂O), Europium oxide (Eu₂O₃), and Nickel nitrate hexahydrate (Ni(NO₃)₂·6H₂O) were taken as the starting materials. All the metal nitrate precursors used were of Merck with analytical grade (99%) purity. Europium oxide (Eu₂O₃) was obtained from HIMEDIA with 99.99% purity. The precursor solution was prepared using stoichiometric amounts of all the metal nitrates and the required oxides in diluted Nitric acid (HNO₃ (10%)) solution under constant stirring at room temperature. Though iron and nickel nitrates are soluble in DI water, diluted HNO₃ solution is necessarily taken to dissolve bismuth nitrate and europium oxide. Thereafter, tartaric acid with a molar ratio of 1:2 corresponding to the metal nitrates was added as the chelating agent. The solution then turned pale yellow which was stirred continuously for 2 h at 50 °C on the hot plate until all the constituent metal nitrates and oxides are completely soluble. The solution is then transferred to the hot air oven where it was heated at 80 °C until it dries completely to form the brown-coloured amorphous precursor powder. The desired phase was then achieved through calcination at a temperature of 550 °C for 4 h.

2.2. Characterization techniques

The structure of BFO and BEFNO samples were investigated using an X-ray diffractometer (PANalyticalX’pert PRO) with Cu K α radiation. Rietveld refinement analysis and crystal structure determination were done with the aid of FULLPROF Suite and VESTA software respectively. Room temperature Raman and Photoluminescence Spectra were recorded using Horiba LABRam HR800UV Raman Spectrometer. Field Emission Scanning Electron Microscopy (FESEM) (Carl Zeiss Neon-40 FESEM) and High-Resolution Transmission Electron Microscopy (HRTEM) (FEI-FP5022/22Tecnai G2 20 S-TWIN) were employed for morphological analysis. Optical properties were studied using UV–Vis Spectrophotometer (SCHIMAZE-2450). For photocatalytic measurements a 500 ml reactor (Lelesil Innovative systems, India Model 1170) was used. The solution was placed in the central quartz jacket illuminated with a 1000 W MPMVL lamp. For temperature control, the reactor was connected to a water bath (Lauda Thermostat-RA8 Make Germany).

3. Results and discussion

3.1. Structural analysis

Preliminary structural investigation of all the samples carried out by X-Ray diffraction (XRD) shows the formation of single-phase with polycrystalline nature as shown in Fig. 1 (a). All the peaks of pure BFO are indexed perfectly according to the standard JCPDS card no. (71–2494). The characteristic doublet reflections from (104) and (110) at 2 θ ~32° suggest the formation of a rhombohedrally distorted R3c structure of BFO. It is clear from the XRD patterns of BEFNO (x = 0.03, 0.05, 0.07) that the most intense peaks at (104) and (110), which are clearly separated in case of pristine BFO, seem to gradually merge and form a broad peak. This indicates induced distortion in the lattice due to

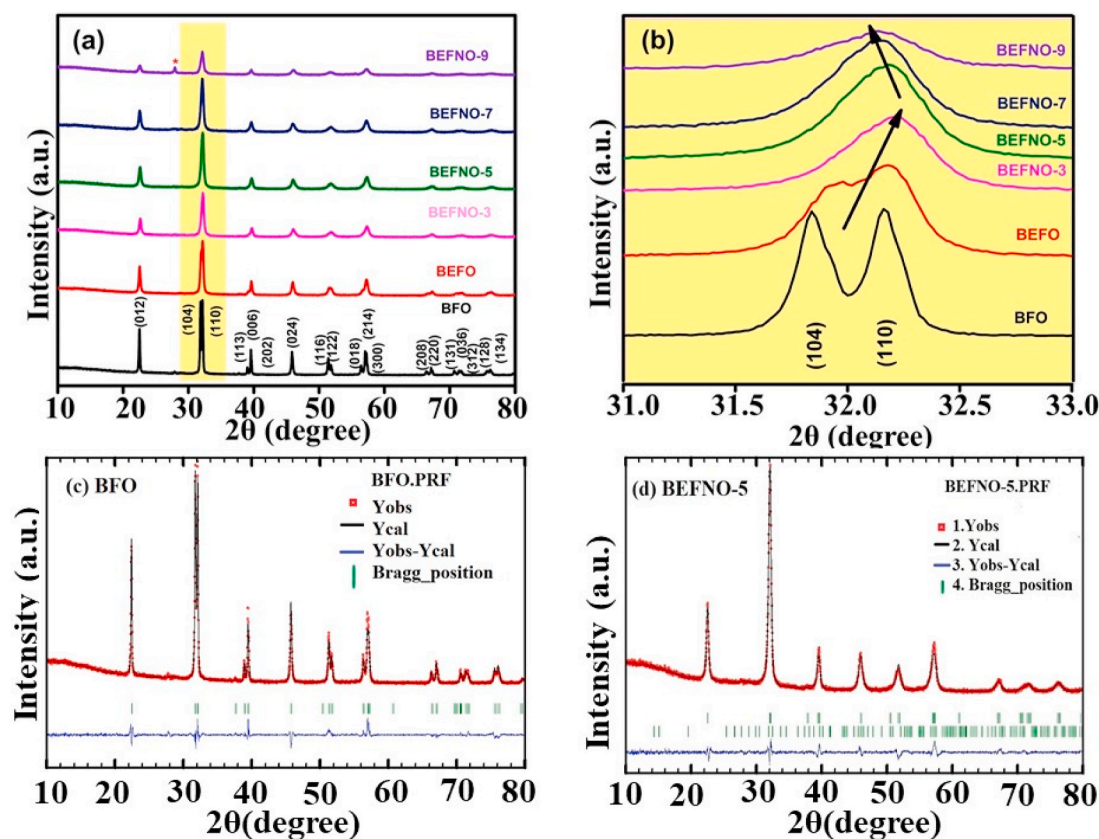


Fig. 1. (a) XRD patterns of BFO, BEFO ($\text{Bi}_{0.96}\text{Eu}_{0.04}\text{FeO}_3$) and $\text{Bi}_{0.96}\text{Eu}_{0.04}\text{Fe}_{1-x}\text{Ni}_x\text{O}_3$ ($x = 0.03, 0.05, 0.07, 0.09$) samples. *sign indicates the presence of impurity corresponding to $\text{Bi}_{25}\text{FeO}_{40}$. (b) Magnified image of doublet peak at about 32° , showing peak merging and shifting with the increase of dopant concentration. Rietveld Refinement of (c) BFO and (d) BEFNO-5 nanostructures.

Table 1

Structural parameters of BFO and the co-substituted samples obtained from Rietveld Refinement and the other relevant formulas.

	BFO	BEFNO-3	BEFNO-5	BEFNO-7
Lattice parameters (A)	R3c a = b = 5.578 c = 13.848	R3c a = b = 5.567 c = 13.730 Pnma a = 5.580 b = 7.831 c = 5.582	R3c a = b = 5.592 c = 13.851 Pnma a = 5.592 b = 7.848 c = 5.581	R3c a = b = 5.579 c = 13.863 Pnma a = 5.661 b = 7.940 c = 5.616
Volume _{cell} (Å ³)	372.732	R3c :368.598 Pnma :243.965	R3c : 372.986 Pnma :244.512	R3c :374.190 Pnma :252.507
Bond Length (A)	Fe-O:2.1876 1.8266 Bi-O:2.3103	R3c Fe-O: 2.1086 1.8303 Bi-O: 2.4021 Pnma Fe-O1: 1.9948 Fe-O2: 2.0114 Bi-O1: 2.5151 Bi-O2: 2.4272	R3c Fe-O: 2.1073 1.8345 Bi-O: 2.4110 Pnma Fe-O1: 1.9970 Fe-O2: 2.0123 Bi-O1: 2.5188 Bi-O2: 2.4375	R3c Fe-O: 2.1098 1.8366 Bi-O: 2.4137 Pnma Fe-O1:2.0026 Fe-O2: 2.0128 Bi-O1: 2.5193 Bi-O2: 2.4415
Bond Angle, θ (deg)	Fe-O-Fe:161.79	R3c Fe-O-Fe:156.02 Pnma Fe-O1-Fe:157.768 Fe-O2-Fe:157.169	R3c Fe-O-Fe: 156.185 Pnma Fe-O1-Fe:157.651 Fe-O2-Fe:157.152	R3c Fe-O-Fe:156.187 Pnma Fe-O1-Fe: 157.745 Fe-O2-Fe:157.164
χ^2	2.6	1.46	1.85	2.66
R _{wp}	15.5	14.7	14.8	18.7
R _p	20	19.3	18.9	23.3
Crystallite size (nm)	35.52	16.26	15.60	15.29
Tolerance factor	0.8437	0.840	0.8399	0.8393
Strain	0.016	0.00823	0.00966	0.00816

doping. However, a slight trace of impurity for 9% Ni doped sample, indicates the gradual formation of multiple phases. The impurity is identified as $\text{Bi}_{25}\text{FeO}_{40}$ and is marked as ‘*’ in Fig. 1(a). There are various reports on the structural transformation of doped BFO from rhombohedral (R3c) to other phases like orthorhombic, tetragonal, or cubic phases [32,36]. Considering the magnified view of reflections of all the samples at $2\theta \sim 32^\circ$ in Fig. 1(b), we observe the peak shifts towards higher angle for Eu-doped BFO (BEFO), caused by the doping at ‘A’ site ($\text{Bi}^{3+} = 1.03 \text{ \AA}$) with smaller Eu^{3+} (0.947 \AA) ion and change in the interplanar spacing as well as grain size effects [37].

However, the co-doped samples exhibit a peak shift towards the higher angle till 5% of Ni doping. Thereafter, with further increase in doping, there is a peak shift towards the lower angle which may be attributed to the larger mismatch between the ionic radii of Ni^{2+} (0.69 \AA) and Fe^{3+} (0.64 \AA) ions [32]. The peak broadening and shifts clearly indicate the substitution of respective dopant ions at ‘A’ and ‘B’ sites. For further confirmatory analysis, Rietveld Refinement was carried out for all the diffraction patterns (up to $x = 7\%$) using the rhombohedral (R3c) model for pristine BFO and a mixed structural model (R3c + Pnma) for the co-substituted samples. A reliable Goodness of Fit (GOF) value (< 3) was observed with (R3c + Pnma) structure fitting, hence proving the co-existence of both the phases in all the substituted samples. The lattice parameters and structural parameters such as bond lengths, bond angles, cell volume and other refined parameters namely R_{wp} , R_p and χ^2 are extracted from Rietveld Refinement analysis, and presented in Table 1. The representative structure of BEFNO-5, with two phases is drawn with the help of VESTA software and displayed below in Fig. 2.

The lattice parameters and estimated cell volume of the samples are found to increase with the gradual increment of ‘Ni’ ion concentration. The ‘Ni’ doping also affects the bond-lengths between Bi, Fe and O atoms while maintaining almost same bond angle. The change in the Fe–O bond-lengths could be caused by the distortion in the FeO_6 octahedron due to ‘Ni’ ion doping which subsequently affects the Bi–O bond length. The average crystallite size was calculated using the Debye-Scherrer formula, and found to be 35.52 nm for BFO. The systematic decrease of crystallite size of co-substituted compounds may be due to the presence of ‘Ni’ ion in the Fe^{3+} site, which acts as an impurity in the crystal and induces anisotropy and suppresses the crystallite growth [28]. The stability of perovskites calculated using Goldschmidt tolerance factor, was found to be 0.84 for pure BFO, which is pretty close to the reported value of 0.88 in literature [38]. This confirms the stability of

synthesized perovskite nanostructures. The substitution of a larger Ni^{2+} ion in place of Fe^{3+} , decreases the value of the tolerance factor, suggesting a higher degree of buckling of the oxygen octahedron. The values of crystallite size and tolerance factor have been listed in Table 1.

3.2. Morphological studies

The morphology of BFO and BEFNO-5 nanostructures were studied using Field Emission Scanning Electron Microscopy (FESEM) and High Resolution Transmission Electron Microscopy (HRTEM) micrographs are shown in Fig. 3. The FESEM images clearly show the formation of inhomogeneous and irregular shape of BFO Fig. 3(a) as well as BEFNO-5 Fig. 3(b). A particular shape for any particle could not be noticed in the FESEM micrographs. However, BEFNO-5 nanoparticles were observed to be more porous than pristine BFO. The induced porosity with the substitution must have increased the surface area of the particles hence affecting many of its properties. The elemental composition was confirmed through Energy Dispersive Analysis of X-Ray (EDAX), displayed in Fig. 3(c-d). Fig. 3(e-f) shows the HRTEM micrograph of BEFNO-5 along with its lattice fringes and d-spacing. The lattice fringes as observed belonged to both the phases present in BEFNO-5 and thus it verifies the XRD results. The d-spacing corresponding to (104) and (200) planes belong to the rhombohedral and orthorhombic phase respectively.

3.3. Raman spectra analysis

Raman spectra is a sensitive technique employed to notice the atomic displacements, lattice distortions, and phase transitions and is generally studied for confirmation of data obtained from XRD and Rietveld analysis. Fig. 4(a–b) shows the room-temperature Raman spectra of BFO and BEFNO-5 samples recorded in the range of $100\text{--}800 \text{ cm}^{-1}$. The peak positions below 100 cm^{-1} cannot be observed due to the rejection of the notch filter in the spectrometer. Theoretical calculations based on Group theory have predicted a total of 20 phonon modes for BFO, out of which 13 ($4A_1+9E$) are both Raman and IR active, $5A_2$ modes are silent and two (A_1+E) are acoustical modes [39,40]. The A_1 modes are polarised along the z-axis whereas the E modes in the x-y plane. The Raman spectra of all the samples are deconvoluted into its Gaussian components and the peak positions are presented in Table 2. As presented in Table 2, only 10 Raman active modes ($4A_1+6E$) could be seen for pristine BFO

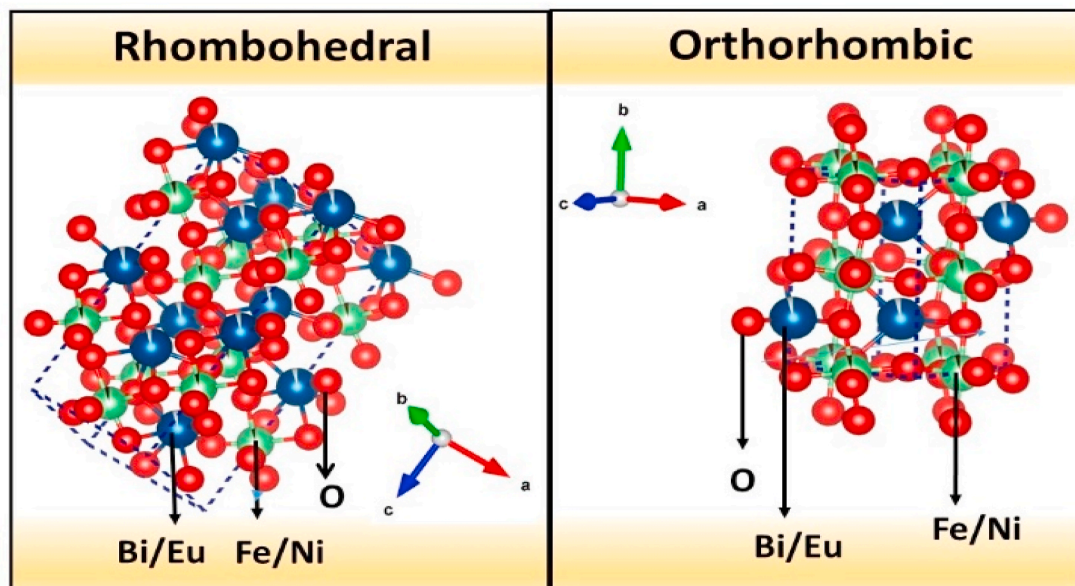


Fig. 2. Structural Representation of BEFNO-5 nanoparticles drawn with the help of VESTA Software.

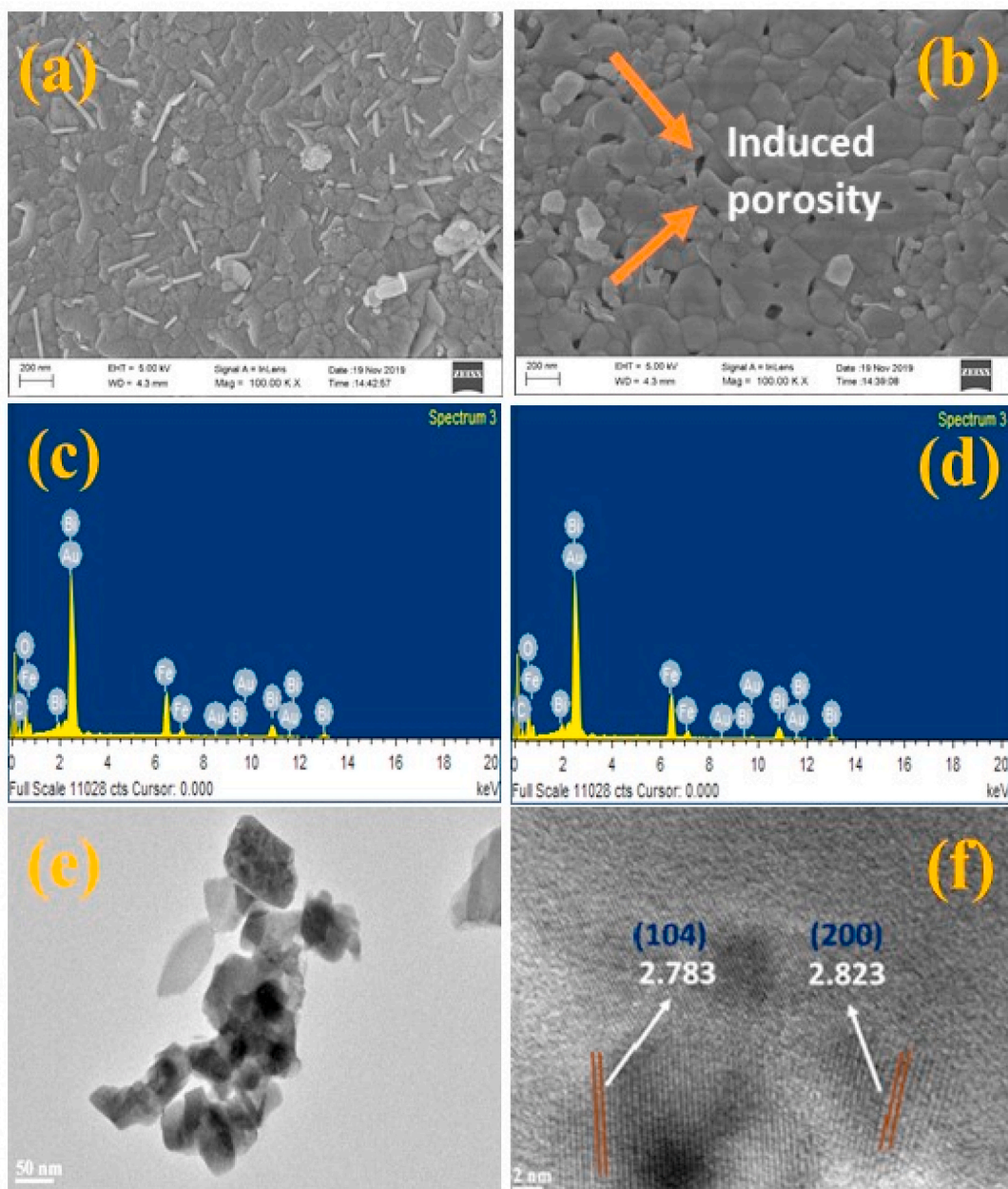


Fig. 3. (a) FESEM micrograph of BFO and (b) of BEFNO-5 nanostructures. EDAX elemental graphs for (c) BFO and (d) BEFNO-5 respectively. (e) HRTEM image of BEFNO-5 nanostructure (f) lattice fringes with d-spacings for two planes belonging to the Rhombohedral and Orthorhombic phase respectively.

sample, confirming the R3c structure [11,41]. However, the spectra of co-substituted samples show a relatively different feature compared to pristine BFO with a reduction in intensity, peak shifting as well as the absence of some modes as compared to pure BFO.

Since the Raman vibrational frequencies are dependent on factors such as force constant and reduced mass by the relation $f = (k/M)^{1/2}$, where k is the force constant, associated with the bond strength and ' M ' is the reduced mass. The shifting of modes to higher frequencies may be caused by the decrease in the average mass at 'A' as well 'B' site [42]. The observed peak broadening of A_1-1 and A_1-2 modes also indicates the change in phonon behaviour due to lattice anharmonicity and distortion produced in the 'Bi' site [43]. Nadeem *et al.* [11] have associated the frequencies lower than 162 cm^{-1} to 'Bi' atoms, $162-262\text{ cm}^{-1}$ to 'Fe' atoms, and above 262 cm^{-1} to 'O' atoms. The change in intensity of low-frequency modes associated with Bi-O bonds, maybe due to the increase in dispersion in Bi-O bond lengths [44]. The low-frequency modes are associated with the relative motion of A-site cations against

the oxygen octahedra, and hence their shifting can be the confirmation of 'A' site substitution with 'Eu'. This phenomenon is due to the chemical pressure-induced bond shortening and lattice distortion arising due to the lattice mismatch between the host and the dopant ion [42]. The hardening of high frequency 'E' modes may be attributed to the oxygen vacancies created by the substitution of ' Fe^{3+} ' site with ' Ni^{2+} ' ions [12]. Arora *et al.* have also claimed that the shifting, broadening, and merging of Raman modes with increasing the dopant concentration is due to the lattice distortion produced as a result of competition between the rhombohedral and orthorhombic phase [45]. The disappearance of A_1-4 and E_4 mode is reportedly attributed to the structural transition from rhombohedral to orthorhombic phase [45]. However, the presence of A_1-1 , A_1-2 , and A_1-3 modes still confirm the existence of the rhombohedral phase [44]. Hence, Raman spectra analysis supports the XRD and Rietveld refinement results, which confirm the co-existence of rhombohedral and orthorhombic phase. The appearance of wide bands at 480 cm^{-1} and 620 cm^{-1} for BEFNO-7 could be associated with distortion

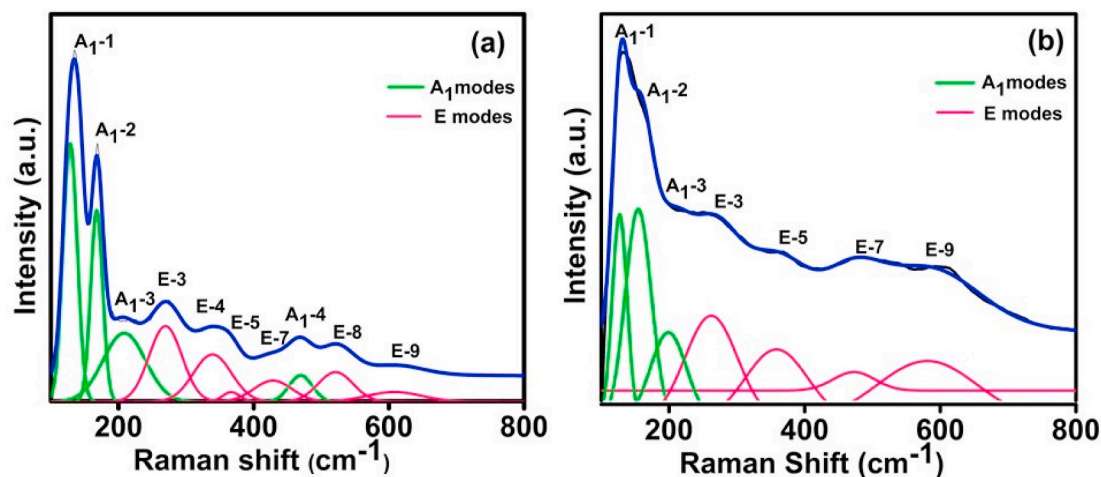


Fig. 4. (a–b): Room Temperature Raman modes of BFO and BEFNO-5 respectively and its deconvolution into A_1 and E modes.

Table 2

Raman modes with exact values of Raman shifts obtained from deconvolution of acquired Spectra for BFO, BEFNO-3, BEFNO-5, and BEFNO-7 nanoparticles.

Sample name/Raman modes	A_1-1	A_1-2	A_1-3	E-3	E-4	E-5	A_1-4	E-7	E-8	E-9
BFO	128	166	212	271	340	367	430	470	521	610
BEFNO-3	139	169	228	270	–	368	–	479	531	610
BEFNO-5	132	169	201	285	–	375	–	475	–	585
BEFNO-7	141	166	229	272	–	374	–	482	539	616

of FeO_6 octahedra [46].

3.4. Chemical –state analysis

To investigate the chemical state of various elements present, X-Ray Photoelectron Spectroscopy (XPS) was carried out and for BEFNO-5 sample (displayed in Fig. 5(a–d)). All of the obtained spectra were fitted with the aid of the CasaXPS MFC Application. The two main characteristic peaks of bismuth centered at 164.5 eV and 159.2 eV, as shown in Fig. 5(a), is ascribed to Bi $4f_{5/2}$ and Bi $4f_{7/2}$ respectively and is due to Bi–O bonds [47].

The presence of the two peaks confirm the Bi^{3+} oxidation state in BEFNO-5. The valence state spectra of ‘Eu’ in Fig. 5(b) confirms the presence of Eu^{3+} oxidation state. Peaks representing Eu $3d_{3/2}$ and Eu $3d_{5/2}$ at 1164.34 eV and 1135.27 eV respectively match quite well with previous reports [48]. The deconvoluted spectra of ‘Fe 2p’ in Fig. 5(c) clearly shows the presence of two doublet peaks centered at 710.12 eV and 723.4 eV arising due to spin-orbit interaction. Both the peaks can be assigned to Fe–O bond [47]. Spin-orbit splitting energy as calculated from the results is ~ 13.28 eV which is comparable to the theoretical value of 13.6 eV for Fe_2O_3 . The presence of satellite peaks at ~ 8 eV higher than the Fe $2p_{3/2}$ peak explains the dominance of Fe^{3+} state of iron. The simultaneous presence of Fe^{2+} state along with Fe^{3+} maybe due to the charge compensation phenomena. The XPS for ‘Ni’ could not be found, though its presence in the samples was confirmed through EDAX analysis in Fig. 3(d). The O1s spectra in (Fig. 5(d)) shows the presence of 3 peaks at 529.7 eV, 531.3 eV, and 532.4 eV, which may be ascribed to O–X (X = metal) bonds, oxygen vacancies, and surface adsorbed oxygen respectively [31].

3.5. Optical elucidation

To study the detailed analysis of optical properties of BFO and the co-substituted samples, UV–Vis as well as Photoluminescence Spectroscopy (PL) studies were carried out. Fig. 6 shows the Energy vs. Absorbance plot for BFO and $Bi_{0.96}Eu_{0.04}Fe_{1-x}Ni_xO_3$ ($x = 0.03, 0.05, 0.07$)

nanoparticles. The obtained spectra clearly show the increase in the absorption intensity in the visible region as well as a slight red-shift of the absorption edge for the co-substituted compounds. The energy bandgaps of the samples are estimated using the Tauc’s Relation given by $(\alpha h\nu)^2 = A(E_g - h\nu)^n$ where ‘ α ’ is the Absorption constant, ‘ $h\nu$ ’ is the energy of the incident photon, ‘ E_g ’ is the bandgap of the material that is to be determined, ‘A’ is the scaling constant and ‘n’ is factor dependant on the type of semiconductor material. The exponent ‘n’ is $\frac{1}{2}$ for indirect bandgap semiconductors and 2 for direct bandgap semiconductors. Since BFO is a direct bandgap semiconductor, the bandgap is determined by linear extrapolation of the curve between $h\nu$ and $(\alpha h\nu)^2$ to the abscissa. The inset of Fig. 6 shows the plots of the bandgap energy of BFO and BEFNO-5 nanoparticles. The table in the inset of Fig. 6 displays the value of band-gap energy and Urbach energy.

There is a slight decrease in the value of the bandgap until $x = 0.05$, but with a further increase in the concentration of ‘Ni’ the bandgap is almost close to that of the pristine BFO. The distortion of the FeO_6 octahedra, change in the bond angle or the rearrangement of the molecular orbitals upon doping may be one of the causes of the decrease in the band gap energy [28]. Xu et al. [49] have also explained this phenomenon based on the creation of oxygen vacancies on substitution of with divalent Ni^{2+} ions in place of trivalent Fe^{3+} ions. The creation of oxygen vacancies may have created localized impurity levels within the bandgap of the material, below the conduction band. The holes formed as a result of charge conservation, occupy the upper part of valence band as an acceptor band, and the impurity level locates itself below the conduction band, hence the band gap decreases with initial concentrations. But as the dopant concentration increases, more holes are formed, increasing the width of the acceptor band and thus increasing the rate of recombination of e-h pairs, which ultimately leads to the narrowing of the oxygen vacancy donor band. A slight increase in the Urbach energy, deduced from the graph between $\ln \alpha$ vs. $h\nu$, corroborates the increase of oxygen vacancies on increasing the Ni^{2+} doping concentration. Moreover, one transition corresponding to the crystal field of Fe^{3+} is observed just below the absorption edge. The absence of another reported transition is due to the limitations of the instrument. Hence, these transitions

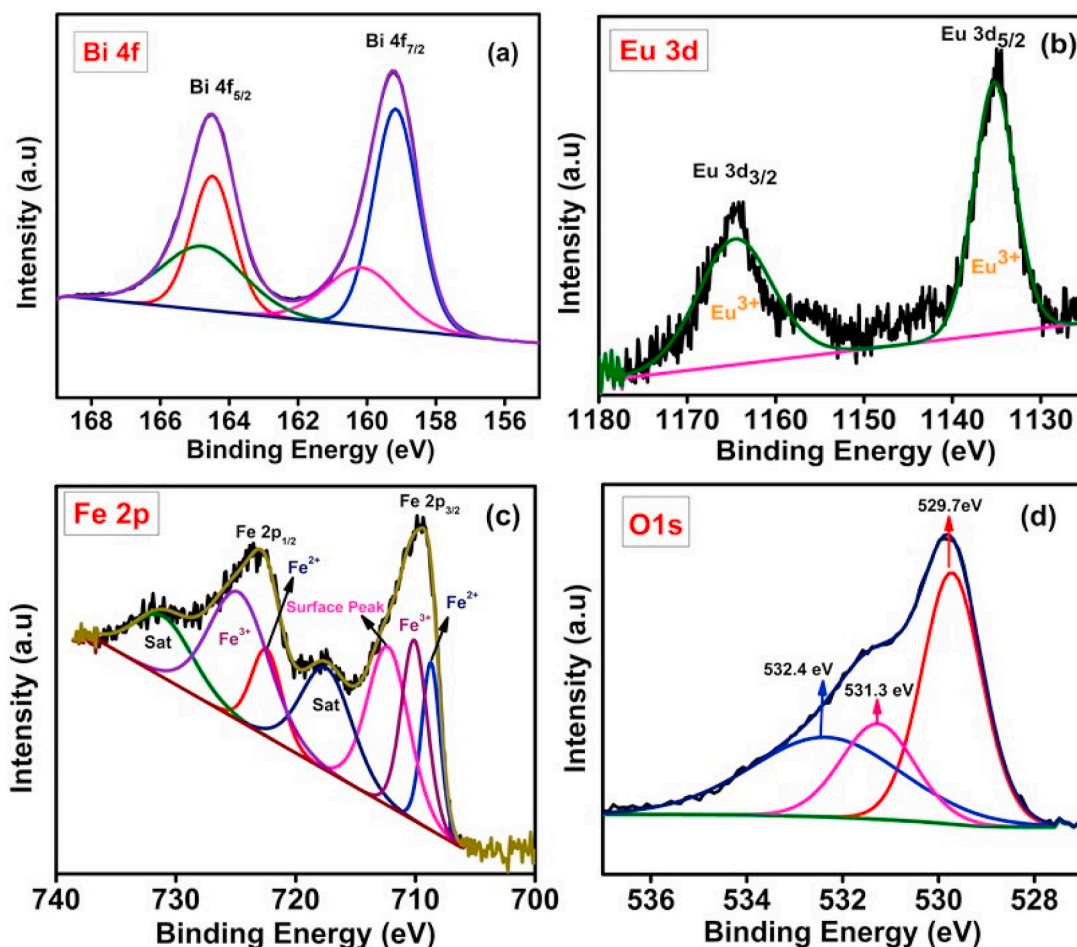


Fig.5. (a–d): XPS Spectra of Bi 4d, Eu 3d, Fe 2p, and O 1s of BEFNO-5 sample.

are studied in detail through PL spectroscopy.

Around six d-d transitions are expected between 0 and 3 eV [46,47]. The two intense transition peaks at about 1.3 eV and 2.0 eV seen in Fig. 7 (a) can be ascribed to on-site Fe^{3+} Crystal-field transitions, ${}^6\text{A}_{1g} \rightarrow {}^4\text{T}_{2g}$ and ${}^6\text{A}_{1g} \rightarrow {}^4\text{T}_{1g}$ respectively [43,50,51]. These transitions are very much sensitive to FeO_6 octahedra distortion, the change in the local environment of Fe^{3+} ion, Fe–O bond length, and Fe–O–Fe exchange interaction, and hence a slight shift in the transition energies can be noticed in BEFNO-5 spectra. The lattice distortion and change in bond-lengths due to in-complete phase transition are also evident from XRD as well as Raman spectra analysis, The shoulder centered at ~ 2.57 eV, the gap absorption threshold, is driven by Fe1 3d – Fe2 3d interstice electron transfer.

The low intensity transitions at 2.65, 2.76 and 3.01 eV can be designated to ${}^6\text{A}_1({}^6\text{S}) \rightarrow {}^4\text{E}({}^4\text{G})$, ${}^6\text{A}_1({}^6\text{S}) \rightarrow {}^4\text{E}_2({}^4\text{D})$ and oxygen defects respectively [37]. The presence of oxygen defects has also been evident from XPS results. The peak around ~ 3.13 eV is attributed to the charge transfer (CT) excitations, which is associated with the inter-atomic O 2p – Fe 3d transition. The occurrence of p-d CT transitions at 3.13 eV is confirmed by the reported value of ~ 3.3 eV [51]. A similar kind of absorption band was also observed for rare-earth substituted BFO compounds, which indicates that their electronic energy level scheme looks similar to that of BEFNO [29,31]. Using several correlations and sub-group analysis, it has been reported that upon symmetry breaking of high-spin Fe^{3+} ions from O_h to C_{3v} (schematically shown in Fig. 8(a)).

The energy levels of Fe^{3+} free ion (d^5 system) splits into t_{2g}^3 and e_g^2 high spin configuration with a crystal field splitting energy separation of $\Delta_0 = 10 Dq$. In the rhombohedral environment, these energy levels

again transform into $a_1^1 e^2 e^2$ electronic configuration, but maintain the energy difference of $\Delta_0 = 10 Dq$ between the highest and the lowest state. With the aid of VB-XPS, the valence band edge was also estimated for BEFNO-5 sample (shown in the inset of Fig. 7(a)).

An electronic band diagram for BEFNO-5 has been proposed in Fig. 8 (b), with the possible electronic transitions elucidated from PL Spectroscopy. With E_v in the energy scale considered at 0 eV, the fermi energy level is located at 1.17 eV as estimated from VB-XPS data. The other observed transitions such as ${}^4\text{T}_{2g}$, ${}^4\text{E}(4\text{G})$ and ${}^4\text{E}_2(4\text{D})$ have also been indicated in the proposed band structure. Besides this, using the two crystal field transition energies, attempts have been made to estimate the value of Δ_0 i.e. energy band gap. This process was completed with Tanabe-Sugano diagram for d^5 systems [52]. The electron repulsion parameter B_{avg} and Δ_0 are found out to be 0.0975 eV and 2.145 eV respectively. The calculated band gap for BFO almost matches with the value obtained from UV–Vis studies.

3.6. Photocatalytic activity

The photocatalytic activity of BFO and $\text{B}_{0.96}\text{Eu}_{0.04}\text{Fe}_{1-x}\text{Ni}_x\text{O}_3$ ($x = 0.03, 0.05, 0.07$) nanoparticles were studied through the degradation of 2-nitrophenol, which is a very harmful industrial pollutant. Initially, a blank solution with 50 mg/L of pollutant (2-nitrophenol) in 200 mL of DI water was irradiated with light for 120 min. To attain the adsorption-desorption equilibrium, the catalyst was stirred in the pollutant solution in the dark for 30 min, before being irradiated in the photocatalytic reactor. As evident from Fig. 9(a), there is almost no degradation seen for the blank solution. With the initial concentration of the pollutant at 50 mg/L, it was elucidated that the degradation efficiency of all the

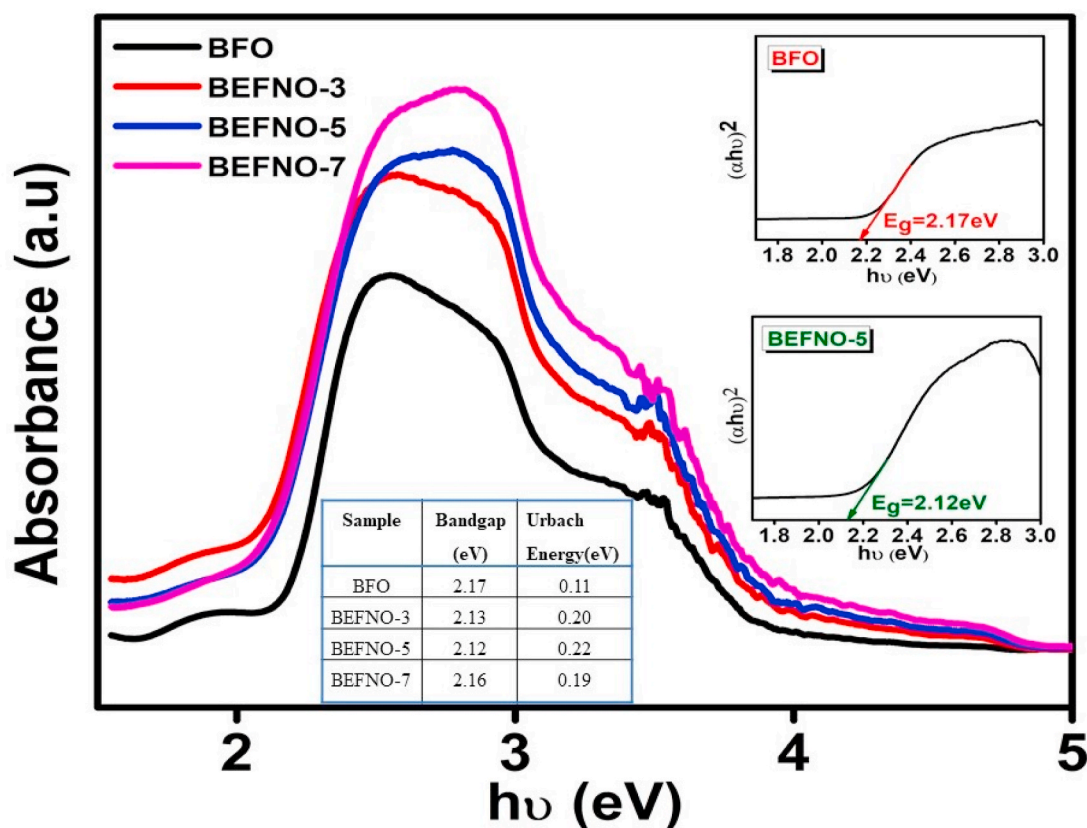


Fig. 6. UV-Vis Spectra of BFO and $\text{Bi}_{0.96}\text{Eu}_{0.04}\text{Fe}_{1-x}\text{Ni}_x\text{O}_3$ ($x = 0.03, 0.05, 0.07$) samples. Insets: Band-Gap estimation of BFO and BEFNO-5 samples using Tauc's Plot, and Table with the information regarding bandgap and Urbach energy of all the samples.

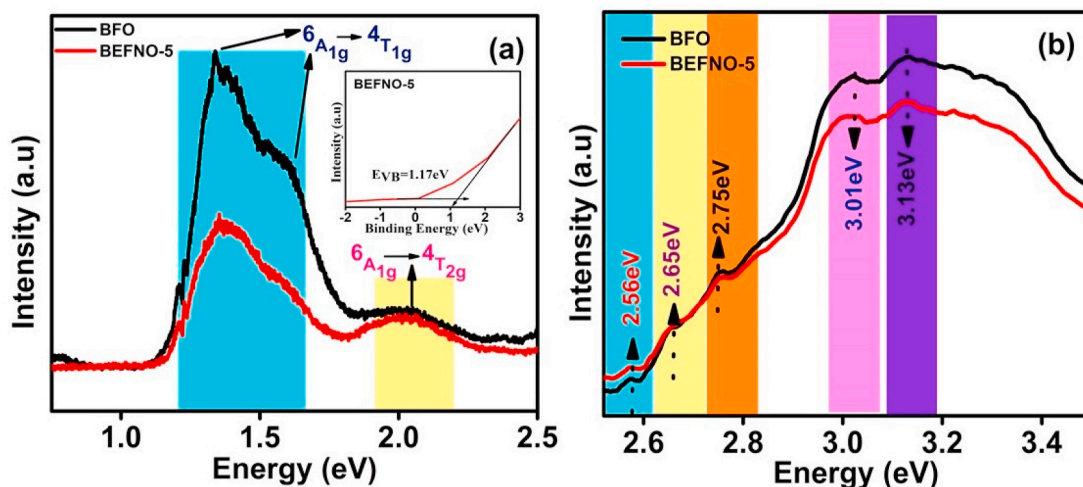


Fig. 7. (a–b): Photoluminescence Spectra and transitions for BFO and BEFNO-5 compounds in the lower and higher energy range respectively. Inset to Fig. 7(a) Valence band edge calculation from VB-XPS for BEFNO-5 nanoparticles.

substituted nanoparticles is higher as compared to pristine BFO. The excellent adsorption of the catalyst on all the samples, may be due to the highly porous nature of the samples, as observed from the FESEM micrographs also. The degradation percentages are calculated for all the samples and the variation has been shown in the form of a histogram in Fig. 9(b). The degradation percentage was seen to be increasing on the substitution of BFO with 'Eu' and 'Ni' till 5% of Ni doping, to about 99.26% in 120 min. Thereafter, on increasing the dopant concentration there has been a decrease in the photocatalytic activity.

The percentage of degradation reduces to 96.78% with 7% of 'Ni' doping. So taking the BEFNO-5 sample as the best catalyst, we also tested its photocatalytic activity with 75 mg/L and 100 mg/L solution. Fig. 9(c) clearly shows the best results with pollutant concentration of 50 mg/L of solution. With higher pollutant concentration the efficiency of the catalyst decreases to 89.6% in the case of 75 mg/L and 79.9% in case of 100 mg/L. The kinetics of the reaction is represented in Fig. 9(d). The kinetics of reaction fits the Langmuir-Hinshelwood model. It comes under pseudo-first-order reaction and the rate of the reaction is

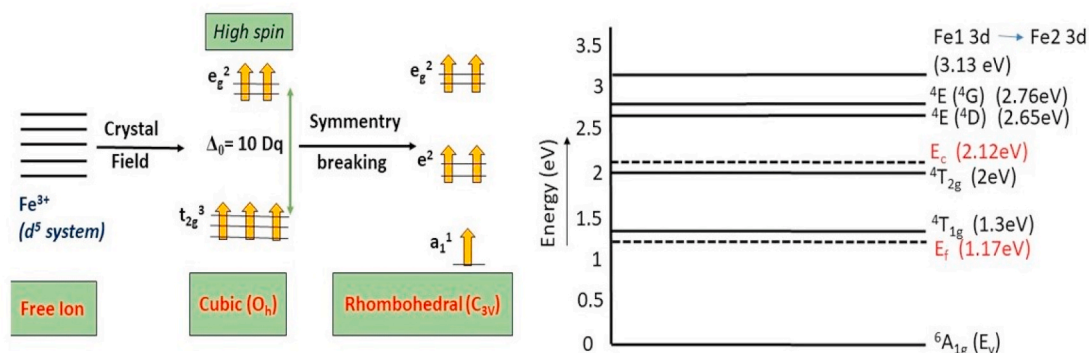


Fig. 8. (a): Schematic representation of symmetry breaking of Fe³⁺ ions in BFO from O_h to C_{3v} phase. (b) Electronic band structure of BEFNO-5 nanoparticles drawn with the help of VB-XPS and PL Spectroscopy.

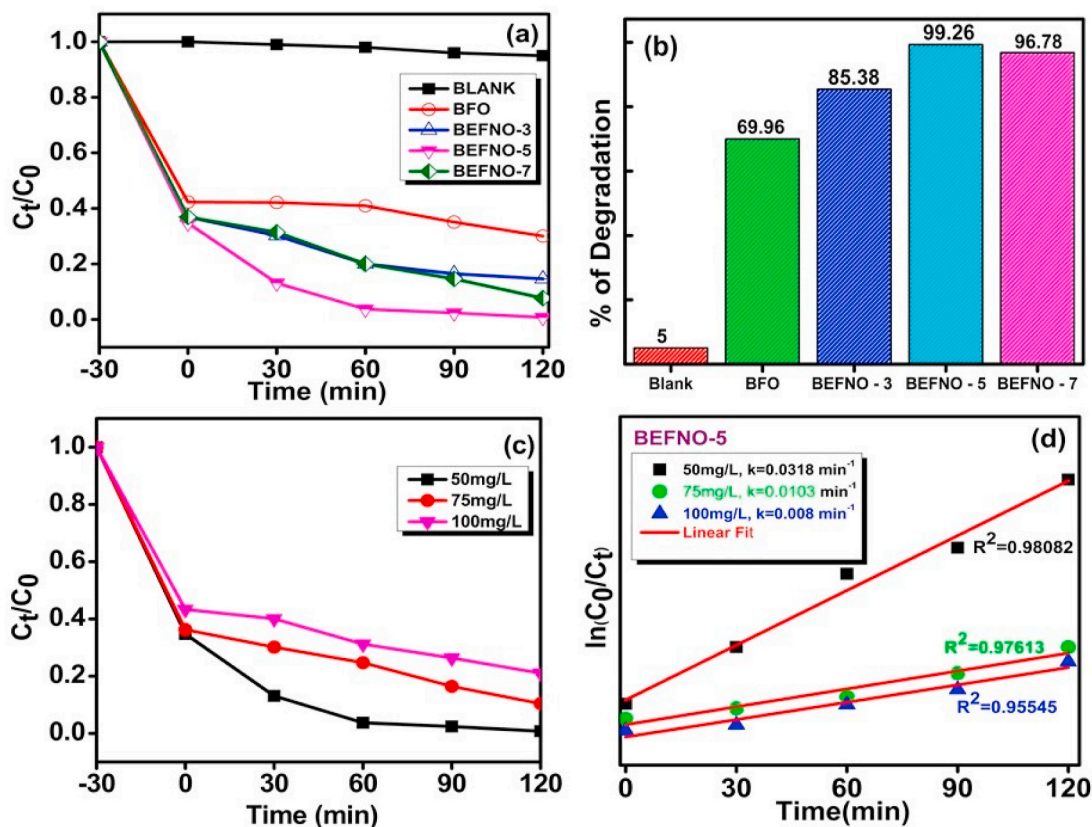


Fig. 9. (a) Photocatalytic activity of BFO as well as Bi_{0.96}Eu_{0.04}Fe_{1-x}Ni_xO₃ (x = 0.03, 0.05, 0.07) as function of irradiation time for the degradation of 2-nitrophenol (50 mg/L). (b) Histogram representing the percentage of degradation of BFO as well as Bi_{0.96}Eu_{0.04}Fe_{1-x}Ni_xO₃ (x = 0.03, 0.05, 0.07), (c) Degradation efficiency of BEFNO-5 with varying concentration of 2-nitrophenol, and (d) Study of the kinetics of reaction for BEFNO-5 with different concentration of 2-nitrophenol.

calculated using the formula:

$$\ln C_0/C_t = kt \quad (1)$$

Here 'k' is the pseudo-first-order rate constant (min⁻¹). The rate constant calculated for 50 mg/L, 75 mg/L and 100 mg/L are 0.0318 min⁻¹, 0.0103 min⁻¹ and 0.008 min⁻¹ respectively for BEFNO-5 nanoparticles. So the reaction rate is best in case of 50 mg/L concentration of the pollutant.

3.6.1. Photocatalytic response

The photocatalytic oxidation process usually involves three steps: (i) Absorption of photons with energy greater than the band-gap energy of the photo-catalyst, (ii) Separation or recombination of the e⁻ and h⁺

pairs, and (iii) Redox reactions on the surface of the photo-catalyst. As observed from the graphs, the substituted BFO nanoparticles serve as better photo-catalyst than the pristine BFO for the degradation of 2-nitrophenol pollutants. This enhanced property can be understood based on certain aspects: (i) Decrease in the band-gap and increase in absorption intensity of the substituted samples which led to the higher absorption of photon energy, (ii) Decreased recombination of photo-generated carriers on the addition of dopant ions which act as trap sites, (iii) Enhancement of surface redox reactions with decreased crystallite size and increased surface area in the case of substituted samples, (iv) Better adsorption effects of the pollutants on the surface of the co-substituted photocatalysts and (v) Narrowing down the surface charge layer thickness [27,30,53–55].

When bismuth ferrite is co-doped with 'Eu' and 'Ni', the dopant ions act as trapping sites for e^- and h^+ pairs to facilitate charge separation and inhibit the recombination process and hence enhance the photocatalytic activity of the catalyst. The impurity donor levels of the material lying below the conduction band acts as trapping sites for electrons and when it lies above the valence band edge, electrons can quench the photogenerated holes [30]. So, the Ni^{2+} dopant ions act as trapping sites for better separation of electrons and holes, those further move towards the surface of the catalyst O_2 to produce reactive O_2^- and $\cdot OH$ radicals. The efficiency of a photocatalyst not only depends on the amount of photon energy absorbed by the catalyst, but also on the extent of adsorption of the pollutant on the surface of the photocatalyst. The energy band-gap of BEFNO-5 being less than pure BFO aids in absorbing more energy than the parent material. Also the adsorption of pollutants on the surface of photocatalyst is maximum for BEFNO-5, owing to its higher porosity as well as increased surface area, hence showing the best photocatalytic activity. However, on further increasing the dopant concentration (more than 5%) might have decreased the distance between the trap sites and thus favoured the recombination process of the charge carriers rather than the separation. Hence, a dopant amount of Ni-5% is the optimal concentration that helps to enhance the photocatalytic mechanism.

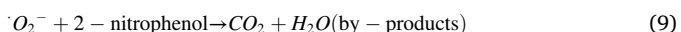
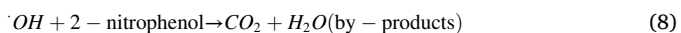
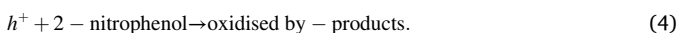
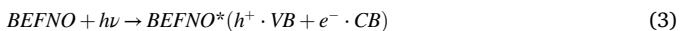
The photo-reactivity and the efficient charge separation and migration of the charge carriers can also be explained based on 'space charge layer thickness'. The thickness of the space charge layer is given by the formula:

$$W = \left[\frac{2\epsilon V_s \epsilon_0}{eN_d} \right]^{1/2} \quad (2)$$

Here 'W' is the thickness of the space charge layer, ϵ and ϵ_0 are the dielectric constants of the medium and air respectively. ' V_s ' is the separation potential, ' e ' is the electronic charge and ' N_d ' is the number of dopant atoms. So the donor concentration plays a crucial role in optimizing the thickness of the space charge layer. An optimum amount of dopant concentration increases the surface barrier and narrows down the space charge layer thickness making it equal to the penetration depth of the light, subsequently facilitating the separation of charge carriers for a better photo-catalytic response. From the PL spectra analysis shown in Fig. 7(a and b), the lower intensity of BEFNO-5 as compared to pristine BFO also validates lesser chances of charge carriers recombination and hence better efficiency [21]. However, beyond the optimum value of donor ions, the space charge layer becomes thinner, and the penetration depth exceeds the space charge layer, and this condition favours the recombination of charge carriers resulting in the decrease of photo-reactivity.

3.6.2. Proposed mechanism

The schematic representation of the proposed mechanism for the photocatalytic degradation of 2-nitrophenol using BEFNO-5 as photocatalyst is shown in Fig. 10 and the step-by-step reaction mechanism is as follows:



When solar light is irradiated on the samples, electron and hole pairs

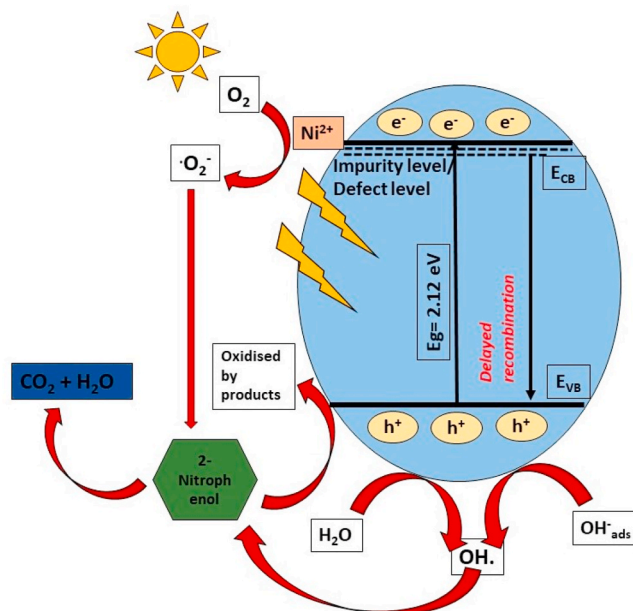


Fig. 10. Schematic representation of the proposed photo-catalytic mechanism in BEFNO-5.

are generated as given in Eq. (3). Holes (h^+) in the VB after moving to the surface of the catalyst, can react with water or surface adsorbed OH^- to produce $\cdot OH$ (Eq. (5) and (6)) or they may directly oxidize the organic pollutants Eq. (4). Simultaneously, surface adsorbed oxygen can now combine with electrons in the CB to form $\cdot O_2^-$ according to Eq. (7). It has been quite broadly recognized that $\cdot O_2^-$ and $\cdot OH$ radicals are extremely reactive species and actively aid in decomposing the organic pollutants to produce harmless by-products. Eventually $\cdot OH$ and $\cdot O_2^-$ radicals mineralize the organic pollutants to produce CO_2 , H_2O , and other harmless inorganic ions as given in Eq. (8) and (9).

4. Conclusion

Europium and Nickel co-doped Bismuth Ferrite nanoparticles were successfully synthesized using the sol-gel method. Structural studies using XRD, Rietveld refinement, and Raman spectroscopy have shown the presence of structural distortion and the presence of rhombohedral (R3c) as well as the orthorhombic (Pnma) phase in the doped compounds. A change in bond length and bond-angles and a decrease in crystallite size was observed on increasing the doping concentration. The Raman modes of co-substituted samples were found to be with decreased intensity and shifted, indicating successful substitution and structural distortion. The microstructural studies using FESEM have shown agglomerated structures. HRTEM images have well corroborated the XRD results of mixed phases. The chemical state was understood using XPS spectroscopy where it has shown the simultaneous presence of Fe^{2+} with Fe^{3+} ions. It has also given a hint towards the presence of oxygen defects or vacancies. For detailed optical analysis, we have carried out the UV-Vis as well as PL spectroscopy. The band-gap of doped compounds were slightly decreased from 2.17 eV for BFO to 2.12 eV for BEFNO-5 nanoparticles. Thereafter, it slightly increased to 2.16 eV for BEFNO-7. This decrease in band-gap was attributed to the presence of impurity levels below the conduction band. The PL intensity was also seen to decrease with doping indicating slowing down of recombination rate. A schematic band structure has been proposed indicating the fermi level, E_c , E_v and energy levels corresponding to Fe^{3+} ion in BEFNO-5 compound. Finally, the efficiency of BEFNO compounds as photocatalysts were tested through the degradation of 2-nitrophenol. It was found that efficiency was enhanced after doping with BEFNO-5 giving the best results with 99.26% of degradation efficiency. The

enhancement in photocatalytic activity was maybe attributed to decreased charge recombination rate (as evident from PL spectroscopy also) upon the induction of dopants as trap states. On increasing the pollutant concentration from 50 mg/L to 75 and 100 mg/L, and BEFNO-5 as the photocatalyst, we have found the best degradation efficiency with 50 mg/L. The rate kinetics fitting into the Langmuir-Hinshelwood model was also best for 50 mg/L of the pollutant.

Author contributions

- J. Nanda and Subhra S. Brahma: Formulation of Research problem and Methodology.
- Subhra S. Brahma: Synthesis of Materials.
- Subhra S. Brahma: Characterization and data collection using XRD, FESEM, UV-Vis, PL Spectroscopy.
- Subhra S. Brahma, Anup Ananga Das and Naresh K. Sahoo: Photocatalysis experiment and data collection.
- Subhra S. Brahma and B. Naik: XPS and HRTEM.
- Subhra S. Brahma: Data analysis and original draft preparation
- J. Nanda and Subhra S. Brahma: Reviewing and Editing the paper

Declaration of competing interest

The authors declare that they have no known competing financial interests or personal relationships that could have appeared to influence the work reported in this paper.

Acknowledgment

This work is supported by SERB, Department of Science and Technology, Government of India (FILE NO. EMR/2016/007046).

References

- [1] H. Lee, H.S. Kim, O.Y. Gong, J.Y. Kim, J.H. Kim, J.S. Choi, H.S. Jung, J.Y. Park, D. H. Kim, Y.S. Seo, T. Choi, Enhanced ferroelectric photovoltaic effect in semiconducting single-wall carbon nanotube/BiFeO₃ heterostructures enabled by wide-range light absorption and efficient charge separation, *J. Mater. Chem. A* 8 (2020) 10377–10385, <https://doi.org/10.1039/d0ta00116c>.
- [2] B.G. Catalan, J.F. Scott, *Physics and Applications of Bismuth Ferrite*, 2009, pp. 2463–2485, <https://doi.org/10.1002/adma.200802849>.
- [3] D. Sando, A. Agbelele, D. Rahmedov, J. Liu, P. Rovillain, C. Toulouse, I.C. Infante, A.P. Pyatakov, S. Fusil, E. Jacquet, C. Carrétéro, C. Deranlot, S. Lisenkov, D. Wang, J.M. Le Breton, M. Cazayous, A. Sacuto, J. Juraszek, A.K. Zvezdin, L. Bellaiche, B. Dkhil, A. Barthélémy, M. Bibes, Crafting the magnonic and spintronic response of BiFeO₃ films by epitaxial strain, *Nat. Mater.* 12 (2013) 641–646, <https://doi.org/10.1038/nmat3629>.
- [4] S. Chakraborty, M. Pal, Highly efficient novel carbon monoxide gas sensor based on bismuth ferrite nanoparticles for environmental monitoring, *New J. Chem.* 42 (2018) 7188–7196, <https://doi.org/10.1039/c8nj01237g>.
- [5] S. Irfan, Z. Zhuanghao, F. Li, Y.X. Chen, G.X. Liang, J.T. Luo, F. Ping, Critical review: bismuth ferrite as an emerging visible light active nanostructured photocatalyst, *J. Mater. Res. Technol.* 8 (2019) 6375–6389, <https://doi.org/10.1016/j.jmrt.2019.10.004>.
- [6] V.A. Khomchenko, V.V. Shvartsman, P. Borisov, W. Kleemann, D.A. Kiselev, I. K. Bdkin, J.M. Vieira, A.L. Kholkin, Effect of Gd substitution on the crystal structure and multiferroic properties of BiFeO₃, *Acta Mater.* 57 (2009) 5137–5145, <https://doi.org/10.1016/j.actamat.2009.07.013>.
- [7] K. Chakrabarti, K. Das, B. Sarkar, S.K. De, Magnetic and dielectric properties of Eu-doped BiFeO₃ nanoparticles by acetic acid-assisted sol-gel method, *J. Appl. Phys.* 110 (2011), <https://doi.org/10.1063/1.3662178>.
- [8] A.I. Iorgu, F. Maxim, C. Matei, L.P. Ferreira, P. Ferreira, M.M. Cruz, D. Berger, Fast synthesis of rare-earth (Pr³⁺, Sm³⁺, Eu³⁺ and Gd³⁺) doped bismuth ferrite powders with enhanced magnetic properties, *J. Alloys Compd.* 629 (2015) 62–68, <https://doi.org/10.1016/j.jallcom.2014.12.108>.
- [9] D. Kothari, V.R. Reddy, A. Gupta, D.M. Phase, N. Lakshmi, S.K. Deshpande, A. M. Awasthi, Study of the effect of Mn doping on the BiFeO₃ system, *J. Phys. Condens. Matter* 19 (2007), <https://doi.org/10.1088/0953-8984/19/13/136202>.
- [10] J. Mao, X. Quan, J. Wang, C. Gao, S. Chen, H. Yu, Y. Zhang, Enhanced heterogeneous Fenton-like activity by Cu-doped BiFeO₃ perovskite for degradation of organic pollutants, *Front. Environ. Sci. Eng.* 12 (2018) 2–11, <https://doi.org/10.1007/s11783-018-1060-9>.
- [11] M. Nadeem, W. Khan, S. Khan, S. Husain, A. Ansari, Tailoring Dielectric Properties and Multiferroic Behavior of Nanocrystalline BiFeO₃ via Ni Doping, 2018, p. 164105, <https://doi.org/10.1063/1.5050946>.
- [12] J.S. Park, Y.J. Yoo, J.S. Hwang, J. Kang, B.W. Lee, Y.P. Lee, J.S. Park, Y.J. Yoo, J. S. Hwang, J. Kang, B.W. Lee, Y.P. Lee, Enhanced Ferromagnetic Properties in Ho and Ni Co-doped BiFeO₃ Ceramics Enhanced Ferromagnetic Properties in Ho and Ni Co-doped BiFeO₃ Ceramics, 2014, 013904, <https://doi.org/10.1063/1.4860296>.
- [13] S. Gupta, M. Tomar, V. Gupta, Ferroelectric photovoltaic properties of Ce and Mn codoped BiFeO₃ thin film, *J. Appl. Phys.* 115 (2014), <https://doi.org/10.1063/1.4859575>.
- [14] P.R. Vanga, R.V. Mangalaraja, M. Ashok, Effect of (Nd, Ni) co-doped on the multiferroic and photocatalytic properties of BiFeO₃, *Mater. Res. Bull.* 72 (2015) 299–305, <https://doi.org/10.1016/j.materresbull.2015.08.015>.
- [15] Q. Yao, X. Xu, S. Peng, Y. Zhu, Z. Wang, Y. Ma, X. Wang, W. Mao, X. Li, Structural, optical and multiferroic properties of Eu, Ba co-doped BiFeO₃, *J. Mater. Sci. Mater. Electron.* 28 (2017) 463–467, <https://doi.org/10.1007/s10854-016-5543-9>.
- [16] Y. Zhu, C. Quan, Y. Ma, Q. Wang, W. Mao, X. Wang, J. Zhang, Y. Min, J. Yang, X. Li, W. Huang, Effect of Eu, Mn co-doping on structural, optical and magnetic properties of BiFeO₃ nanoparticles, *Mater. Sci. Semicond. Process.* 57 (2017) 178–184, <https://doi.org/10.1016/j.mssp.2016.10.023>.
- [17] K. Chakrabarti, K. Das, B. Sarkar, S. Ghosh, S.K. De, G. Sinha, J. Lahtinen, Enhanced magnetic and dielectric properties of Eu and Co co-doped BiFeO₃ nanoparticles, *Appl. Phys. Lett.* 101 (2012) 1–6, <https://doi.org/10.1063/1.4738992>.
- [18] S.D. Lakshmi, I.B.S. Banu, Tailoring the multiferroic properties of BiFeO₃ by co-doping Er at Bi site with aliovalent Nb, Mn and Mo at Fe site, *Appl. Ceram. Technol.* 16 (2019) 1622–1631, <https://doi.org/10.1111/ijac.13201>.
- [19] M. Umar, N. Mahmood, RSC Advances Rationally Designed La and Se Co-doped Bismuth Ferrites with Controlled Bandgap for Visible Light Photocatalysis, 2019, pp. 17148–17156, <https://doi.org/10.1039/c9ra03064f>.
- [20] C.M. Raghavan, J.W. Kim, H.J. Kim, W.J. Kim, S.S. Kim, Preparation and properties of rare earth (Eu, Tb, Ho) and transition metal (Co) co-doped BiFeO₃ Thin Films, *J. Sol-Gel Sci Technol.* 64 (2012) 178–183.
- [21] F.B. Li, X.Z. Li, The enhancement of photodegradation efficiency using Pt-TiO₂ catalyst, *Chemosphere* 48 (2002) 1103–1111, [https://doi.org/10.1016/S0045-6535\(02\)00201-1](https://doi.org/10.1016/S0045-6535(02)00201-1).
- [22] M.Y. Ghalay, T.S. Jamil, I.E. El-Seesy, E.R. Souaya, R.A. Nasr, Treatment of highly polluted paper mill wastewater by solar photocatalytic oxidation with synthesized nano TiO₂, *Chem. Eng. J.* 168 (2011) 446–454, <https://doi.org/10.1016/j.cej.2011.01.028>.
- [23] S. Baruah, M. Jaisai, R. Imani, M.M. Nazhad, J. Dutta, Photocatalytic paper using zinc oxide nanorods, *Sci. Technol. Adv. Mater.* 11 (2010), <https://doi.org/10.1088/1468-6996/11/5/055002>.
- [24] Z. Ye, L. Kong, F. Chen, Z. Chen, Y. Lin, C. Liu, A comparative study of photocatalytic activity of ZnS photocatalyst for degradation of various dyes, *Optik (Stuttg.)* 164 (2018) 345–354, <https://doi.org/10.1016/j.ijleo.2018.03.030>.
- [25] R. Yuan, R. Guan, P. Liu, J. Zheng, Photocatalytic treatment of wastewater from paper mill by TiO₂ loaded on activated carbon fibers, *Colloids Surfaces A Physicochem. Eng. Asp.* 293 (2007) 80–86, <https://doi.org/10.1016/j.colsurfa.2006.07.010>.
- [26] G.J. Lee, J.J. Wu, Recent developments in ZnS photocatalysts from synthesis to photocatalytic applications — a review, *Powder Technol.* 318 (2017) 8–22, <https://doi.org/10.1016/j.powtec.2017.05.022>.
- [27] S. Irfan, L. Li, A.S. Saleemi, C. Nan, Enhanced photocatalytic activity of La³⁺ and Se⁴⁺ co-doped bismuth ferrite nanostructures, *J. Mater. Chem. A Mater. Energy Sustain.* (2017) 1–9, <https://doi.org/10.1039/C7TA01847A>.
- [28] M. Sakar, S. Balakumar, P. Saravanan, S. Bharathkumar, Compliments of confinements: substitution and dimension induced magnetic origin and band-bending mediated photocatalytic enhancements in Bi_{1-x}Dy_xFeO₃ particulate and fiber nanostructures, *Nanoscale* 7 (2015) 10667–10679, <https://doi.org/10.1039/c5nr01079a>.
- [29] Z. Hu, D. Chen, S. Wang, N. Zhang, L. Qin, Y. Huang, Facile synthesis of Sm-doped BiFeO₃ nanoparticles for enhanced visible light photocatalytic performance, *Mater. Sci. Eng. B Solid-State Mater. Adv. Technol.* 220 (2017) 1–12, <https://doi.org/10.1016/j.mseb.2017.03.005>.
- [30] S. Irfan, S. Rizwan, Y. Shen, L. Li, S. Butt, The gadolinium (Gd³⁺) and nanoparticles as new solar light active photocatalyst, *Nat. Publ. Gr.* (2017) 1–12, <https://doi.org/10.1038/srep42493>.
- [31] N. Zhang, D. Chen, F. Niu, S. Wang, L. Qin, Y. Huang, Enhanced visible light photocatalytic activity of Gd-doped BiFeO₃ nanoparticles and mechanism insight, *Nat. Publ. Gr.* (2016) 1–11, <https://doi.org/10.1038/srep26467>.
- [32] M. Nadeem, W. Khan, S. Khan, M. Shoaib, S. Husain, M. Mobin, Significant enhancement in photocatalytic performance of Ni doped BiFeO₃ nanoparticles, *Mater. Res. Express* 5 (2018), 065506, <https://doi.org/10.1088/2053-1591/aac70d>.
- [33] M. Zargazi, M.H. Entezari, A novel synthesis of forest like BiFeO₃ thin film: photoelectrochemical studies and its application as a photocatalyst for phenol degradation, *Appl. Surf. Sci.* 483 (2019) 793–802, <https://doi.org/10.1016/j.apsusc.2019.03.347>.
- [34] X. Shi, S. Quan, L. Yang, G. Shi, F. Shi, Facile synthesis of magnetic Co₃O₄/BFO nanocomposite for effective reduction of nitrophenol isomers, *Chemosphere* 219 (2019) 914–922, <https://doi.org/10.1016/j.chemosphere.2018.12.045>.
- [35] D. Moitra, B.K. Ghosh, M. Chandel, N.N. Ghosh, Synthesis of a BiFeO₃ nanowire-reduced graphene oxide based magnetically separable nanocatalyst and its versatile catalytic activity towards multiple organic reactions, *RSC Adv.* 6 (2016) 97941–97952, <https://doi.org/10.1039/c6ra22077k>.

- [36] T.D. Rao, T. Karthik, S. Asthana, Investigation of structural, magnetic and optical properties of rare earth substituted bismuth ferrite, *J. Rare Earths* 31 (2013) 370–375, [https://doi.org/10.1016/S1002-0721\(12\)60288-9](https://doi.org/10.1016/S1002-0721(12)60288-9).
- [37] S. Chauhan, M. Kumar, S. Chhoker, S.C. Katyal, H. Singh, M. Jewariya, Multiferroic, magnetoelectric and optical properties of Mn doped, *Solid State Commun.* 152 (2012) 525–529, <https://doi.org/10.1016/j.ssc.2011.12.037>.
- [38] J. Sharma, A. Kumar, S. Kumar, Investigation of structural and magnetic properties of Tb – Ni-doped bismuth ferrite nanoparticles by auto-combustion method, *Appl. Phys. A* (2017), <https://doi.org/10.1007/s00339-017-1140-x>.
- [39] H. Khelifi, I. Zouari, S. Habouti, N. Abdelmoula, D. Mezzane, H. Khemakhem, Raman spectroscopy and evidence of magnetic, *J. Alloys Compd.* (2015), <https://doi.org/10.1016/j.jallcom.2015.02.211>, 0–19.
- [40] I.K.N. V. Giridharan, Structural, Optical, and Multiferroic Properties of Single Phased BiFeO₃, vol. 3, 2013, <https://doi.org/10.1007/s00339-013-7712-5>.
- [41] H. Fukumura, H. Harima, K. Kisoda, M. Tamada, Y. Noguchi, M. Miyayama, Raman Scattering Study of Multiferroic BiFeO₃ Single Crystal, vol. 310, 2007, pp. 2006–2008, <https://doi.org/10.1016/j.jmmm.2006.10.282>.
- [42] P. Kumar, C. Panda, M. Kar, Effect of rhombohedral to orthorhombic transition on magnetic and dielectric properties of La and Ti co-substituted, *Smart Mater. Struct.* 24 (n.d.) 45028, <https://doi.org/10.1088/0964-1726/24/4/045028>.
- [43] Y. Liu, J. Wei, Y. Guo, T. Yang, Z. Xu, Phase transition, interband electronic transitions and enhanced ferroelectric properties in Mn and Sm co-doped Bismuth Ferrite films, *RSC Adv.* (2016), <https://doi.org/10.1039/C6RA20740E>.
- [44] R. Barman, S.K. Singh, D. Kaur, Structural phase transition and enhanced ferroelectricity in bi(Fe_{1-x}Mn_x)O₃ thin films deposited by pulsed laser deposition, *Thin Solid Films* (2015), <https://doi.org/10.1016/j.tsf.2015.10.017>.
- [45] A. Bi, S. Chauhan, M. Arora, P.C. Sati, S. Chhoker, S.C. Katyal, M. Kumar, Structural, vibrational, optical, magnetic and dielectric properties of, *Ceram. Int.* (2013) 1–7, <https://doi.org/10.1016/j.ceramint.2013.01.066>.
- [46] A. Lahmar, S. Habouti, M. Dietze, C. Solterbeck, A. Lahmar, S. Habouti, M. Dietze, C. Solterbeck, M. Es-souni, Effects of Rare Earth Manganites on Structural, Ferroelectric, and Magnetic Properties of BiFeO₃ Thin Films Effects of Rare Earth Manganites on Structural, Ferroelectric, and Magnetic Properties of BiFeO₃ Thin Films, 2014, pp. 18–21, <https://doi.org/10.1063/1.3064954>, 012903.
- [47] S. Chauhan, S. Chhoker, S.C. Katyal, M. Singh, Substitution driven structural and magnetic transformation in Ca-doped BiFeO₃ nanoparticles, *RSC Adv.* (2016), <https://doi.org/10.1039/C6RA02316A>.
- [48] X. Song, Y. Ma, X. Ge, H. Zhou, G. Wang, H. Zhang, X. Tang, Y. Zhang, Europium-based in finite coordination polymer nanospheres as an effective fluorescence probe for phosphate sensing †, 2017, pp. 8661–8669, <https://doi.org/10.1039/C6RA27819A>.
- [49] X. Xu, W. Liu, H. Zhang, M. Guo, P. Wu, S. Wang, J. Gao, G. Rao, The Abnormal Electrical and Optical Properties in Na and Ni Codoped BiFeO₃ Nanoparticles The Abnormal Electrical and Optical Properties in Na and Ni Codoped, 2015, p. 174106, <https://doi.org/10.1063/1.4919822>.
- [50] A. Anshul, A. Kumar, B.K. Gupta, R.K. Kotnala, J.F. Scott, A. Anshul, A. Kumar, B. K. Gupta, R.K. Kotnala, J.F. Scott, Photoluminescence and Time-Resolved Spectroscopy in Multiferroic BiFeO₃: Effects of Electric Fields and Sample Aging Photoluminescence and Time-Resolved Spectroscopy in Multiferroic BiFeO₃: Effects of Electric Fields and Sample Aging, 2013, pp. 3–8, <https://doi.org/10.1063/1.4808450>.
- [51] M. Kaur, K.L.Y. Poonam, Multiferroic and optical studies on the effects of Ba²⁺ ions in BiFeO₃ nanoparticles, *J. Mater. Sci. Mater. Electron.* (2016), <https://doi.org/10.1007/s10854-016-4320-0>, 0–7.
- [52] D.M. Sherman, The electronic structures of Fe³⁺ coordination sites in iron oxides: applications to spectra, bonding, and magnetism, *Phys. Chem. Miner.* 12 (1985) 161–175, <https://doi.org/10.1007/BF00308210>.
- [53] S. Fatima, S.I. Ali, M.Z. Iqbal, Congo red dye degradation by graphene nanoplatelets/doped bismuth ferrite nanoparticle, hybrid catalysts under dark and light conditions, *Catalysts* 10 (2020) 367, <https://doi.org/10.3390/catal10040367>.
- [54] S. Fatima, S.I. Ali, D. Younas, A. Islam, D. Akinwande, S. Rizwan, P. Article, Graphene Nanohybrids for Enhanced Catalytic Activity and Large Surface Area, 2018, pp. 1–10, <https://doi.org/10.1557/mrc.2018.194>.
- [55] M.A. Iqbal, S.I. Ali, F. Amin, A. Tariq, M.Z. Iqbal, S. Rizwan, La- and Mn-codoped bismuth ferrite/Ti₃C₂MXene composites for Efficient photocatalytic degradation of Congo red dye, *ACS Omega* 4 (2019) 8661–8668, <https://doi.org/10.1021/acsomega.9b00493>.